Mesostructure - thermoelectric properties relationships in VxMn1-xSi1.74 (x=0, 0.04) higher manganese silicides prepared by magnesiothermy

Sylvain Le Tonquesse, Vincent Dorcet, Loïc Joanny, Valérie Demange, Carmelo Prestipino, Quansheng Guo, David Berthebaud, Takao Mori, Mathieu Pasturel

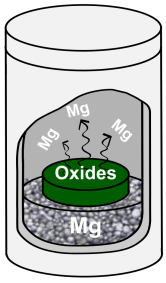

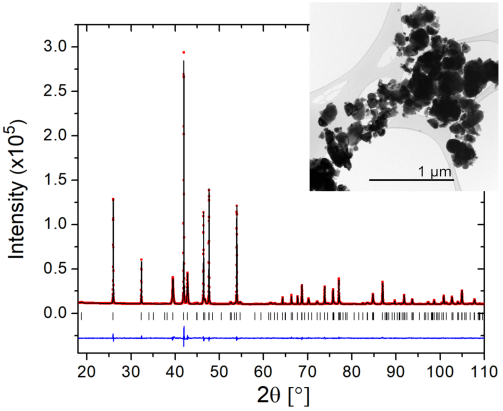

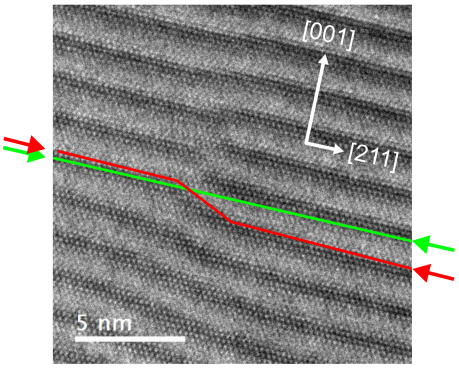

Mesostructure - thermoelectric properties relationships in $V_xMn_{1-x}Si_{1.74}$ (x = 0, 0.04) Higher Manganese Silicides prepared by magnesiothermy

Sylvain Le Tonquesse[a], Vincent Dorcet[a], Loic Joanny[a], Valérie Demange[a], Carmelo Prestipino[a], Quansheng Guo[b], David Berthebaud[b], Takao Mori[c], Mathieu Pasturel[a,]

[a]*Univ Rennes, CNRS, ISCR-UMR6226/ScanMAT-UMS2001, F-35000, Rennes, France*
[b]*CNRS - Saint-Gobain - NIMS, UMI3629, Laboratory for Innovative Key Materials and Structures (LINK), National Institute for Materials Science, 1-1 Namiki, Tsukuba, Ibaraki 305-0044, Japan*
[c]*National Institute for Materials Science (NIMS), WPI-MANA and CFSN, Tsukuba, Japan*

Abstract

The synthesis of pure pristine and vanadium-doped $MnSi_\gamma$ (γ = 1.74) powder by a relatively fast, 'low temperature' and high yield magnesioreduction process is described. The powder obtained by this innovative route is composed of well crystallized grains with sizes ranging from 20 to 500 nm and free from any MnSi precipitates. Mesostructured densified pellets with average grain sizes as small as 550 nm are obtained by spark plasma sintering (SPS). Detailed structural and microstructural characterization of the samples were realized at every stage of the process, highlighting a high concentration of defects such as orientational or spacing anomalies of the Nowotny phase, γ variations within a single grain and dislocations. Accordingly a significant decrease of the lattice thermal conductivity is evidenced in comparison to conventionally synthesized (arc-melting/SPS) samples having similar density and (V/)Mn/Si stoichiometry. The thermoelectric properties of these materials are discussed in regard of their complex microstructure.

Keywords: Intermetallics, thermoelectric materials, chemical synthesis, crystal structure, transmission electron microscopy

*mathieu.pasturel@univ-rennes1.fr

1. Introduction

Thermoelectric (TE) materials are being extensively investigated for their potential of energy-saving and dynamical energy harvesting through solid state conversion of heat into electricity [1, 2]. Higher Manganese Silicides (HMS) with chemical formula $MnSi_\gamma$ ($1.72 < \gamma < 1.75$) are widely considered as a promising thermolectrical material because of their potential in industrial application. Indeed, HMS are low density materials composed of non-hazardous and inexpensive elements and they possess very good mechanical properties and oxidation resistance. HMS are currently used as *p*-type material for industrial thermoelectric generator (TEG) prototypes operating at mid-temperature [3, 4]. However, a large scale industrial implementation of such materials is limited by their moderate thermoelectric properties usually evaluated by the figure-of-merit *ZT* defined as:

$$ZT = \frac{\alpha^2}{\rho(\kappa_L + \kappa_e)}T \tag{1}$$

where α is the Seebeck coefficient, ρ the electrical resistivity, κ_L and κ_e the lattice and electronic contribution to the total thermal conductivity κ and T the operating temperature.

Improvement of their TE properties can be achieved through various strategies enhancing ZT [5, 6]. Many studies have been focused on chemical doping of $MnSi_\gamma$ to increase the power factor $PF = \alpha^2/\rho$ [7, 8] or on fabrication of elaborated microstructures with the aim to decrease κ_L *via* synthesis routes such as ball-milling [9], melt-spinning [10, 11], fast combustion [12] or reactive sintering [13, 14]. For example, ZT_{max} exceeding unity has been obtained for Re supersaturated HMS realized by liquid quenching [15, 16] at the expense of industrial scalability and elevated price of Re.

Investigation of HMS is rather difficult because these materials are characterized by a high structural, microstructural and synthesis complexity. This

includes (i) the difficulty to obtain pure samples due to the incongruent melting of $MnSi_\gamma$ [17] and the high vapor pressure of Mn at elevated temperature [18], (ii) the formation of metallic MnSi precipitates inside HMS grains which can severely affect the TE [19, 20] and mechanical [21] properties, (iii) the incommensurate chimney-ladder crystal structure which is often unsatisfactorily described as a series of commensurate Mn_ySi_x structures (x, y are natural numbers) [22], and (iv) the anisotropic transport properties which can bias the comparison of performances in the case of crystallographically textured samples [23].

Recently, we reported on the synthesis of high purity mesostructured TE skutterudites by magnesioreduction of oxides [24]. This scalable process based on cheap and air-stable oxides leads to the formation at moderate temperature of well crystallized submicronic powders with elevated TE properties. Similar process was attempted to obtain HMS powders by Girard *et al.* [25] starting from nanosilica and MnO_2 in molten salt fluxes but the information on such process is limited to a single conference abstract and, to the best of our knowledge, no peer-review article has ever been published. We have thus applied a flux-free magnesioreduction process employing MnO and Si as reactants for the synthesis of pure and vanadium doped $MnSi_{1.74}$. The structural and microstructural characterizations, using X-ray diffraction Rietveld refinements in a composite crystal structure model, electron backscattering diffraction and scanning/transmission electron microscopy on both as-synthesized powders and spark plasma sintered pellets are presented thereafter. The thermal dependence of the electrical resistivity, Seebeck coefficient and thermal conductivity have been measured in the temperature range 300-800 K and subsequent thermoelectric performances are discussed in terms of structure-microstructure-properties relationships. These results are compared to equivalent HMS prepared by conventional melting-solidification-annealing method.

2. Experimental procedure

For the magnesioreduction (MR) synthesis of $MnSi_{1.74}$ and $V_{0.04}Mn_{0.96}Si_{1.74}$, precursor mixtures first need to be prepared by ball-milling of V_2O_5 (Merck, 99 %), MnO (Alfa Aesar, 99 %) and Si (Ventron, 99.9 %) with a molar ratio of 0 : 1 : 1.74 and 0.02 : 0.96 : 1.74, respectively, under air in a planetary mill (Retsch PM100) for 3 h at 650 rpm in a WC vial filled with Ø 10 mm WC balls (fig 1a). A small ball-to-powder ratio of 5 : 1 is used in order to avoid contamination by WC during the milling process. The obtained precursor mixture is cold-pressed at 65 MPa into Ø 10 mm pellets with about 4 mm height. Each pellet is placed in a Mo-crucible with Mg turnings (Strem Chemicals, $\geq$ 99 %) equally distributed under and on top of the pellet (fig. 1b). Such distribution of Mg helps to maximize the surface contact between Mg and the pellets in order to promote a homogeneous reduction and was found compulsory to avoid the presence of Mg_2Si by-product. A 25 % excess Mg is empirically needed to complete the magnesioreduction reaction:

$$MnO + 1.74\ Si + \underset{(+25\%)}{Mg} \longrightarrow MnSi_{1.74} + MgO \tag{2}$$

A graphite seal is inserted between the crucible and the lid and the system is held tight with a clamping system. This set-up is placed in an Inconel tube filled with Ar to avoid the Mo-crucible oxidization. The whole is heated up to 1173 K at a rate of 60 K h^{-1} in a tubular furnace and held at this temperature for 8 h before being cooled down by switching off the furnace (fig. 1c). At the end of the reaction the product still in the shape of a pellet can be easily separated from loose MgO powder (fig. 1d). A black powder composed of $MnSi_\gamma$ is obtained by softly crushing the pellet in an agate mortar. The MgO by-product is removed by soaking the as-synthesized powder twice in diluted hydrochloric acid (2 wt.%) for 5 - 10 minutes and washing three times with distilled water and once more with ethanol before being dried at 353 K overnight (fig.1e). The washed $MnSi_\gamma$

powder is then densified by spark plasma sintering (SPS) in Ø 10 mm graphite dies at 1273 K and 75 MPa for 20 min with 100 K min^{-1} heating/cooling rates using a FCT HP-D-10 apparatus.

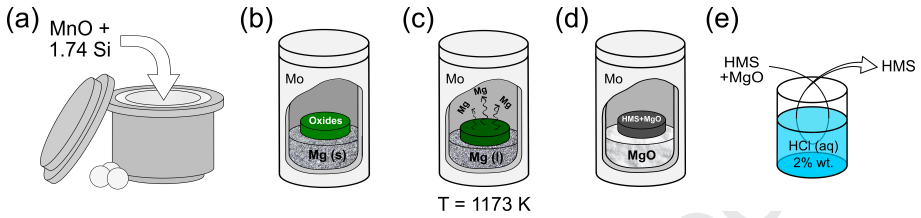

Figure 1: Main steps of the magnesioreduction synthesis: (a) MnO and Si are ball-milled in WC vial; (b) pellets of MnO/Si mixture are sealed with the adequate amount of Mg in a Mo crucible; (c) Mg vapor reduces the oxides during the heat treatment at 1173 K; (d) the reduction is completed after 8 h at 1173 K; (e) MgO is removed from the product by soaking the powder in diluted HCl.

In order to investigate how magnesiothermy synthetic route affects the final thermolectric properties, $MnSi_{1.74}$ has also been synthesized by conventional fusion solidification method. Stoichiometric amounts of the elements are arc-melted (AM) three times to ensure homogenization and the obtained ingot was annealed for 100 h at 1273 K in evacuated silica tubes. The annealed ingot was finely ground in an agate mortar and the powder was densified by SPS in Ø 10 mm graphite dies at 1238 K and 80 MPa for 5 min.

The crystal structure and purity of the samples were checked by powder X-ray diffraction (PXRD) using a Bruker D8 Advance diffractometer in the Bragg-Brentano geometry working with a monochromatized Cu Kα_1 radiation (λ = 1.5406 Å) and equipped with a LynxEye detector. Structural parameters were determined by Rietveld refinement of the PXRD patterns using JANA2006 [26]. Scanning electron microscopy (SEM) images, energy dispersive spectroscopy (EDS) and electron backscattering diffraction (EBSD) were performed using a JEOL JSM 7100F microscope equipped with an Oxford EDS SDD X-Max spectrometer and an EBSD HKL Advanced Nordlys Nano detector. TEM analyses were performed on a JEOL 2100 LaB_6 instrument operating at 200 kV and equipped with an Oxford EDS SDD 80 mm^2 spectrometer and high resolution Gatan US1000 and Orius 200D cameras. Preparation of the powder samples for SEM analyses con-

sisted in their deposition on carbon tape followed by metallization with carbon. For transmission electron microscopy (TEM), a small amount of powder was sonicated in absolute ethanol and deposited for drying on a carbon coated copper grid. For EBSD and EDS analyses, densified pellets were consecutively mirror polished with 320 down to 1200 grit SiC papers, diamond paste (3 and 1 μm) and colloidal silica. EBSD mappings were analyzed using the *Channel 5* software (HKL Technology). Thin foils of densified pellet for TEM analyses were obtained by dimpling a 100 μm thick pellet down to 10 μm with diamond paste (3 and 1 μm) followed by Ar-ion milling using a Fischione Ion Mill 1010 operating at 4.5 kV and 4.5 mA.

The thermal diffusivity (D) has been measured by the laser flash method on Ø 10 mm and 2 mm thick samples coated with graphite using a Netzsch LFA 467 HyperFlash equipment under N_2 atmosphere. The thermal conductivity could be calculated by the $\kappa = DC_pd$ relation with C_p the specific heat of the sample determined thanks to a Netzsch Pyroceram reference sample and d the density measured by the Archimede method. The Seebeck coefficient and electrical resistivity were measured simultaneously on 6×2×2 mm bars using a ZEM3 device (ULVAC-RIKO Inc., Yokohama, Japan) under He atmosphere.

3. Results and discussion

3.1. Magnesioreduction synthesis

The XRD pattern of the precursor mixture obtained by high energy ball-milling of MnO and Si is shown in fig. 2. Interestingly, MnSi and $MnSi_\gamma$ readily start to form in the milling vial indicating the reduction of manganese. According to the Ellingham diagram [27, 28] the reduction of MnO by Si :

$$2\,MnO + Si \longrightarrow 2\,Mn + SiO_2 \qquad \Delta G_r^\circ(298\ K) = \text{-}136.5\ kJ.mol^{-1} \qquad (3)$$

is thermodynamically possible. The activation energy for this reaction is prob-

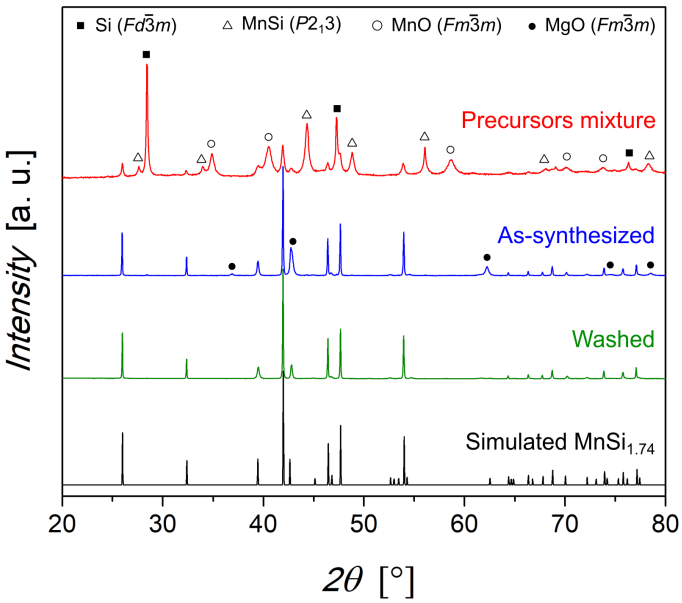

Figure 2: XRD patterns of the precursors mixture (red), as-synthesized HMS powder (blue), HCl washed HMS powder (green) and simulated pattern for $MnSi_{1.74}$ with first order satellite peaks [22] (black). Some weak intensity satellite reflections in the simulated pattern might not be visible in the experimental ones because of their large broadening (see text for details).

ably overcome locally in the milling vial when highly energetic shocks occur. Upon further milling, metallic Mn would then react with unreacted Si to form $MnSi_\gamma$ and MnSi as already reported by different groups [29, 30, 31]. SiO_2 must be present in the mixture but could not be detected by XRD due to its probable amorphous nature. At the end of the milling step, a very intimate mixture of Mn- and Si-containing species is produced according to:

$$\mathrm{MnO} + 1.74\mathrm{Si} \xrightarrow[3h]{650rpm} \underset{51\%}{\mathrm{Si}} + \underset{20\%}{\mathrm{MnO}} + \underset{18\%}{\mathrm{MnSi}} + \underset{11\%}{\mathrm{MnSi}_\gamma} (+\mathrm{SiO_2}) \qquad (4)$$

where the molar concentrations are determined from Rietveld refinement (see fig. SI.1 and tables SI 1,2,3,4).

The precursors mixture is then reacted with Mg according to:

$$\underset{51\%}{\mathrm{Si}} + \underset{20\%}{\mathrm{MnO}} + \underset{18\%}{\mathrm{MnSi}} + \underset{11\%}{\mathrm{MnSi}_{\gamma}}\,(+\mathrm{SiO_2}) + \mathrm{Mg} \xrightarrow[8h]{1123K} \mathrm{MnSi}_{\gamma} + \mathrm{MgO} \qquad (5)$$

and XRD on the as-synthesized powders (fig. 2, blue curve) confirms that the product is only composed of $MnSi_{\gamma}$ and MgO.

Magnesioreduction was attempted at several temperatures and a lower limit of 1073 K has been found to initiate this reaction. The high vapor pressure of Mg at these elevated temperatures is expected to easily penetrate inside the pellet to induce the reduction of the oxides and subsequent interdiffusion of native metals to form the targeted silicide. Additionally, the reduction of MnO and SiO_2 by Mg is highly exothermic at 1123 K with ΔH_r = - 346.9 and - 344.0 kJ mol^{-1} respectively [27, 28]. The heat released locally inside the pellet may accelerate the reaction and a scenario close to a combustion synthesis [32, 33] cannot be ruled out.

3.2. Microstructure of the magnesioreduced $MnSi_{\gamma}$ powders

Fig. 3a and 3b show secondary electron SEM images of an as-synthesized MR HMS powder containing $MnSi_{\gamma}$ and MgO. It is composed of grains with sizes ranging from about 50 nm to several hundreds of nm, some of them forming aggregates with micrometric sizes. According to EDS elemental analyses, MgO constitute 60 at.% of the as-synthesized powder. Moreover, they give a Si/Mn metal ratio of about 1.7 which is in agreement with the targeted $MnSi_{1.74}$ composition (fig. SI.2a).

The HMS + MgO composite microstructure has been investigated by TEM. A typical brightfield image of the as-synthesized HMS powder is shown in fig. 4a. EDS analyses and selected area electron diffraction realized on several areas of the sample assign the electron-opaque grains to $MnSi_{\gamma}$ while the more electron-transparent matrix is mainly composed of much smaller MgO crystals. These observations are consistent with the much broader XRD Bragg peaks ascribed

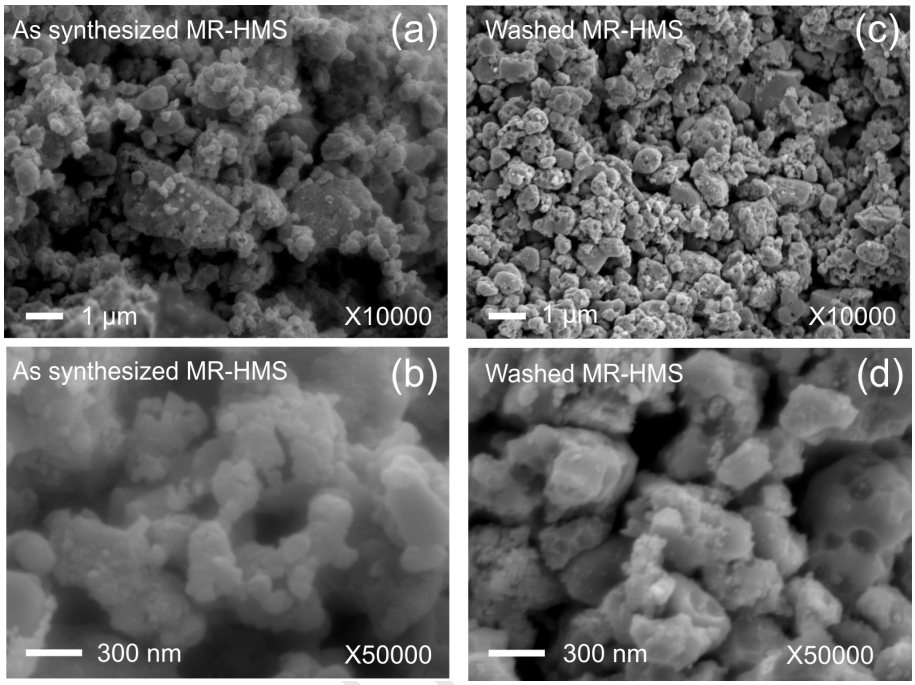

Figure 3: Secondary electron SEM images of (a)(b) as-synthesized MR HMS powder composed of $MnSi_{1.74}$ and MgO and (c)(d) MR HMS powder after acidic washing containing only $MnSi_{1.74}$, at two different magnifications.

to MgO compared to those of HMS (fig. 2). We hypothesize here that the MgO matrix formed during the MR reaction and surrounding the $MnSi_\gamma$ grains plays a significant role by limiting the silicide particle growth at the rather elevated reaction temperature and thus helps stabilizing the powder submicronic size.

After acidic washing, powder XRD (fig. 2) shows that MgO is eliminated, at least down to the detection limit of the technique. The absence of Mg K_α emission line on SEM-EDS analyses and the detection of only traces of Mg on TEM-EDS confirm that MgO was almost entirely removed from the sample (fig. SI.2). Without the surrounding MgO matrix, the morphology of the HMS grains is fully revealed and typical SEM and TEM images are shown in fig. 3c,d and 4b, respectively. The grains have relatively isotropic shapes with sizes ranging from about 50 to few hundreds of nm. Based on their relatively faceted shape, most of the grains look single crystalline. Interestingly, high resolution trans-

mission electron microscopy (HRTEM) does not reveal any MnSi precipitates inside the grains as is usually seen in samples obtained by crystallization from a liquid melt. It should also be noticed that HRTEM observations of the surface of the grains before and after the acidic washing (not shown here) do not reveal any trace of chemical erosion of the grains by the acid. Electron diffraction patterns (fig. 4c) can be fully indexed using 4 Miller indices *hklm* with the $MnSi_{\gamma}$ composite crystal structure described in details in the next section. Noticeable orientation and spacing anomalies as already reported and described by Ye and Amelinckx [34] are clearly visible along the [00*l*] rows and will be further discussed in section 3.4.

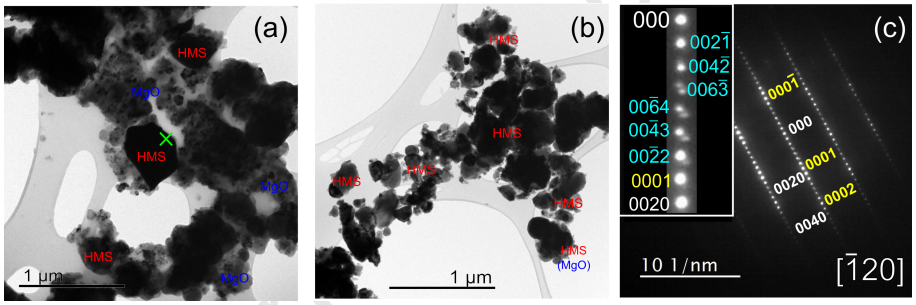

Figure 4: TEM brightfield images of the (a) as-synthesized MR-$MnSi_{\gamma}$ + MgO powder and (b) HCl-washed $MnSi_{\gamma}$ powder. Annotations on the images correspond to the main phase deduced from EDS analyses performed on different spots of the observed area. (c) Selected area electron diffraction patterns taken at the green cross in (a) and indexed with the composite crystal structure of $MnSi_{1.74}$ described in section 3.3 and pictured in fig.5. For clarity reason, only strong reflections corresponding to the two basic subsystems are indicated along the [00l] row but all satellite reflections could be indexed with 00*lm* indices. *hkl0* (white), *hk0m* (yellow) and *hklm* (blue) Miller indices correspond to the Mn-, Si-subsystems and satellite reflections, respectively. The inset shows a close-up view of the orientation anomaly along the [00l] direction.

3.3. Structural analysis of the MR-$MnSi_{\gamma}$ powders

$MnSi_{\gamma}$ crystallizes in a composite tetragonal 'Chimney-Ladder' structure-type - also known as Nowotny phase - in which a 'ladder' subsystem of Si-atoms (*P4/nnc*, no. 126) is penetrating a 'chimney' subsystem of Mn ($I4_1/amd$, no. 141) [35, 36, 37] (fig. 5).

As mentioned above, HMS were originally described as a large family of stoichiometric compositions with formula Mn_ySi_x where x and y are natural

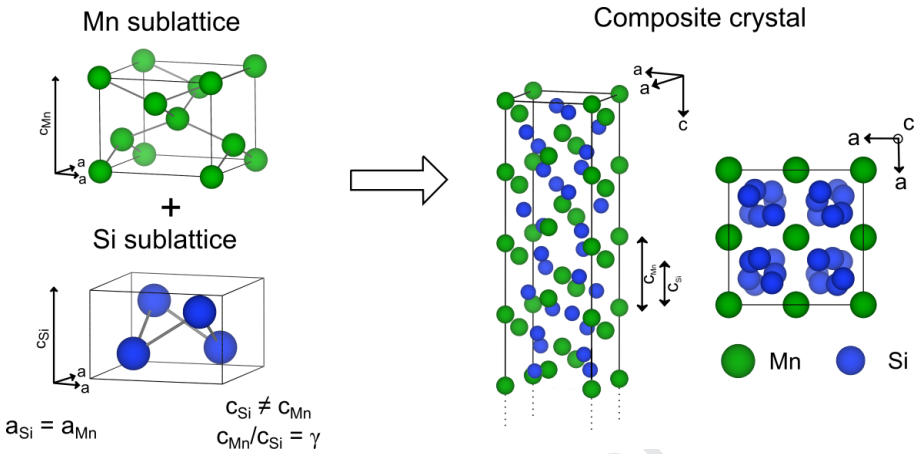

Figure 5: Crystal structure description of $MnSi_\gamma$ showing the interpenetrating tetragonal Mn- and Si-subsystems with identical *a*- but different *c*-lattice parameters (left). The interaction between the two subsystems leads to a composite $MnSi_\gamma$ unit-cell (right) where $\gamma = c_{Mn}/c_{Si}$.

numbers and $\gamma = x/y$ is ranging between ≈ 1.727 and 1.75. Accordingly, they were described as commensurate structure with *c* increasing from 17.4 Å for the simplest Mn_4Si_7 ($\gamma = 1.75$) to $c = 117.9$ Å for $Mn_{27}Si_{47}$ ($\gamma \approx 1.741$). Miyazaki *et al.* have proposed a more general approach, describing $MnSi_\gamma$ as a composite structure with a restrained domain of stability for γ [22]. In this approach, the structure is composed of two incommensurately modulated subsystems, where the modulation results from interactions between mutually incommensurate, periodic subsystems [38, 39]. In the case of $MnSi_\gamma$, each subsystem is described by only one atom in the asymmetric unit (four equivalent in the basic cell). They have identical *a* lattice parameters of about 5.53 Å, while the *c* lattice parameters are different ($c_{Si} \approx 2.5$ Å and $c_{Mn} \approx 4.4$ Å) with a non-rational ratio $\gamma = c_{Mn}/c_{Si}$ that corresponds to the Si/Mn stoichiometry of the compound in the case of full chemical occupancy.

In this context, the 3D lattice periodicity is replaced by a 3D+1 one. The symmetry elements present in the structure are described using a $I4_1/amd(00\gamma)00ss$ superspace group and four *hklm* Miller indices are required for the complete indexing of the diffraction patterns [40]. In this superspace description, the reciprocal basis vectors of the Mn and Si-sublattices in $MnSi_\gamma$ are described from

the basis vectors of the composite crystal lattice via the W matrices:

$$W_{Mn} = \begin{pmatrix} 1 & 0 & 0 & 0 \\ 0 & 1 & 0 & 0 \\ 0 & 0 & 1 & 0 \\ 0 & 0 & 0 & 1 \end{pmatrix} \qquad W_{Si} = \begin{pmatrix} 1 & 0 & 0 & 0 \\ 0 & 1 & 0 & 0 \\ 0 & 0 & 0 & 1 \\ 0 & 0 & 1 & 0 \end{pmatrix} \tag{6}$$

In this setting, the diffraction patterns of $MnSi_{\gamma}$ are composed of *hk00* reflections common to both subsystem, *hkl0* reflections relative to the basic Mn-subsystem, *hk0m* reflections relative to the basic Si-subsystem and *hklm* satellite reflections with contribution of the incommensurate modulations. In incommensurately modulated structures, the displacement vector $u^{\mu}(x,y,z)$ of the μ-atom relative to its base structure position $\bar{x}^{\mu}(x,y,z)$ is described by the modulation vector function $u^{\mu}(v_{\mu})$. The argument v_{μ} of the modulation function is the fourth 3D+1 superspace coordinate of μ in the basic structure. From the respective W matrices, v_{Mn} and v_{Si} are defined by the relations:

$$\begin{aligned} v_{Mn} &= t + \gamma x_3 \\ v_{Si} &= t + 1/\gamma x_4 \end{aligned} \tag{7}$$

where t is a real number corresponding to the initial phase of $u^{\mu}(v_{\mu})$.

As the modulation $u^{\mu}(v_{\mu})$ is periodic in 3D+1 superspace, it can be decomposed by Fourier series according to:

$$u^{\mu}(v_{\mu}) = \sum_{k=1}^{n} A_{\mu}^{k} sin(2\pi k v_{\mu}) + B_{\mu}^{k} cos(2\pi k v_{\mu}) \tag{8}$$

where the amplitudes A_{μ}^{k} and B_{μ}^{k} are refined to fit to the experimental data.

The experimental XRD are satisfactorily fitted by Rietveld refinements using

this approach as shown *e.g.* in fig. 6a for a HCl-washed $MnSi_\gamma$ powder with refined lattice parameters, modulation vector and atomic displacement parameters summarized in Table 1 and 2. The refined γ value of 1.7416(2) is in agreement with the synthesized and EDS determined compositions, confirming the ability of the synthesis technique to produce composition controlled materials.

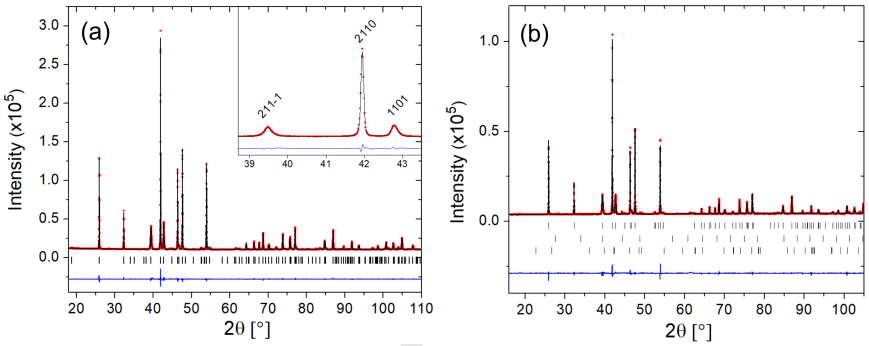

Figure 6: Rietveld refined XRD patterns of (a) washed $MnSi_{1.74}$, with enlarged view in inset, and (b) $V_{0.04}Mn_{0.96}Si_{1.74}$ powders prepared by magnesioreduction. The experimental data are plotted in red symbols, the calculated one in black line and the difference with a blue line. The vertical ticks indicate the theoretical $V_xMn_{1-x}Si_{1.74}$ (x = 0, 0.04) Bragg positions up to the 2^{nd} order satellite reflections. In (b), the second and third rows indicate the theoretical Bragg positions of VSi_2 and MnSi impurities.

In the present case, the collected XRD data allowed satellite reflections up to the 2^{nd} order to be considered in the refinement procedure as many of them were found to have intensities just above the background level. The modulation functions were described using Fourier coefficients up to $n = 2$ and $n = 4$ for Mn and Si subcells, respectively. The large number of refined Fourier coefficients used to describe the Si modulation is imposed by the crystal symmetry, the first coefficient describing the z component of the modulation - B^4 - being non null for $n = 4$. Refined Fourier coefficients are tabulated in Table 2 while the resulting modulation functions are plotted in fig. 7. On the one hand, the displacement of Mn around its average position $\bar{x}^{Mn} = (0,0,0)$ has a small maximum amplitude along z of about 0.04 Å while no displacement is found in the (x,y) plane. On the other hand, Si-atoms at $\bar{x}^{Si} = (\frac{1}{4}, \frac{1}{4}, \frac{1}{4})$ show much larger

Table 1: Structural parameters obtained by Rietveld refinement of washed $MnSi_{1.74}$ and $V_{0.04}Mn_{0.96}Si_{1.74}$ XRD patterns.

		$MnSi_{1.74}$	$V_{0.04}Mn_{0.96}Si_{1.74}$
Mn	$\bar{x}^{Mn}$ (x,y,z)	0 0 0 [1]	0 0 0
	a (Å)	5.52908(2)	5.5301(1)
	c_{Mn} (Å)	4.36749(4)	4.3696(1)
	γ	1.7416(2)	1.7394(2)
	U_{iso} (Å^2)	0.0069(8)	0.001(2)
Si	$\bar{x}^{Si}$ (x,y,z)	0.25 0.25 0.25 [1]	0.25 0.25 0.25
	a (Å)	5.52908(2)	5.5301(1)
	c_{Si} (Å)	2.5077(1) [2]	2.5121(3)
	U_{iso} (Å^2)	0.0033(4)	0.004(2)

[1] Average position coordinates of Mn and Si are constrained
[2] Calculated as c_{Mn}/γ

sinusoidal displacements reaching a maximum of x = y ≈ 0.2 Å and z ≈ 0.08 Å. The large displacement modulations induce the formation of Si-atom helices around the $(\frac{1}{4},\frac{1}{4},z)$ axis as shown in the projection of the crystal structure along the *c*-axis (fig. 5). All these refined values are in very good agreement with those reported by Miyazaki *et al.* obtained on high resolution neutron powder diffraction data of $MnSi_{\approx 1.736}$ synthesized by conventional melting/annealing method [22].

Table 2: Refined coefficients of the modulation functions of Mn (top) and Si (bottom) for washed $MnSi_{1.74}$ and $V_{0.04}Mn_{0.96}Si_{1.74}$

	$MnSi_{1.74}$			$V_{0.04}Mn_{0.96}Si_{1.74}$		
Mn	$x\ (=x_1)$	$y\ (=x_2)$	$z\ (=x_3)$	$x\ (=x_1)$	$y\ (=x_2)$	$z\ (=x_3)$
B[2]	0	0	-0.019(1)	0	0	-0.017(3)
Si	$x\ (=x_1)$	$y\ (=x_2)$	$z\ (=x_4)$	$x\ (=x_1)$	$y\ (=x_2)$	$z\ (=x_4)$
A[1]	0.0764(3)	0.0764(3)	0	0.0773(4)	0.0773(4)	0
B[1]	0.0764(3)	-0.0764(3)	0	0.0773(4)	-0.0773(4)	0
A[3]	0.0099(6)	0.0099(6)	0	0.0107(7)	0.0107(7)	0
B[3]	-0.0099(6)	0.0099(6)	0	-0.0107(7)	0.0107(7)	0
B[4]	0	0	-0.041(3)	0	0	-0.049(4)

As illustrated in the inset to fig. 6 with the intense (2110) and (1101) Bragg

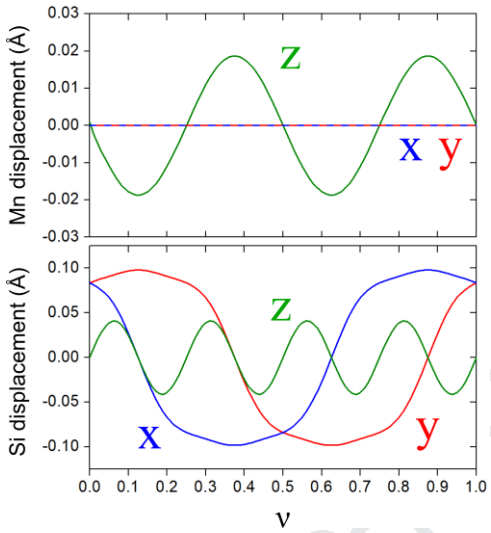

Figure 7: Coordinates of the displacement vector relative to the average position for Mn (top) and Si (bottom) as a function of the fourth space parameter ν for washed $MnSi_{1.74}$

peaks, *hk0m* reflections of the Si subsystem are much broader than the relatively narrow *hkl0* reflections of the Mn subsystem. From the diffractogram refinement point of view, this strong peak shape anisotropy between the different families of reflections has been managed using a strain tensor implemented in JANA2006. This could be attributed to higher disorder on the Si subsystem as confirmed by HRTEM observations that are discussed in next section. This strain tensor also avoids the implementation of an extra Si-position in the structural model proposed by Akselrud *et al.* to describe the disordered Si-subsystem [41].

The XRD pattern of washed $V_{0.04}Mn_{0.96}Si_{1.74}$ powder was also fitted using the same approach (fig. 6b, Tables 1 and 2). The lattice parameters are slightly larger and γ slightly smaller in the case of the V-doped sample. On the other hand, the Fourier coefficient of the modulation functions remains relatively similar. It should be noticed that VSi_2 and MnSi impurities represent 1 and 2 wt.% of the sample, respectively. The presence of VSi_2 suggest that V was not entirely inserted in the structure during the magnesioreduction process.

3.4. Microstructure of sintered $MnSi_\gamma$ pellets

$MnSi_{1.74}$ and $V_{0.04}Mn_{0.96}Si_{1.74}$ pellets with densities of 96 % according to the Archimede weighing were produced by spark plasma sintering. After the sintering step, both samples are single phase according to XRD (fig. 8 and SI.2), indicating that most of the residual VSi_2 and MnSi reacted during the heat treatment for the doped sample. Accordingly, a significant decrease of γ from about 1.74 for the as-synthesized MR powder to 1.73 for the as-sintered pellet is obtained by Rietveld refinements (fig. SI.3), reaching a value close to the arc-melted (AM) samples. Generally, the lattice and structural parameters (table 3) of each composition made by both MR and AM synthesis routes are quite equivalent. Upon V-doping, a moderate increase of a and c_{Mn} is consistent with the slightly larger vanadium metallic radius (r_V = 1.346 Å, r_{Mn} = 1.264 Å[42]) while a much larger increase of c_{Si} from about 2.515 to almost 2.53 Å is in agreement with Miyazaki's results [20]. As can be seen from the 2θ shift of the $(211\bar{1})$ reflection toward low 2θ angles, this increase of c_{Si} is associated to a significantly smaller γ value for V-doped samples.

Interestingly, the $(211\bar{1})$ and (1101) reflections of the AM samples are much less affected by the broadening than MR samples. In the case of the MR V-doped sample, the (1101) peak even seems to be composed of three highly convoluted peaks. This suggests some level of heterogeneity of c_{Si} and thus of γ in the MR samples, in agreement with similar observations reported by Miyazaki *et al.* in V- and Ge-doped HMS prepared by conventional methods [20].

EDS mapping on polished surfaces of the SPSed pellets (fig. SI.4) confirms a homogeneous concentration of Mn and Si (within the resolution of the technique) on the analyzed areas of the $MnSi_{1.74}$ sample, while in the case of $V_{0.04}Mn_{0.96}Si_{1.74}$, a few vanadium-rich areas with diameters below 1 μm could be attributed to small amounts of residual VSi_2 impurity (not visible on XRD patterns). As a consequence, the V-concentration in this $V_xMn_{1-x}Si_{1.74}$ may be slightly below the nominal x = 0.04 value.

Residual porosity with average size of approximately 100 nm and located at

the grain boundaries is visible for samples prepared by MR and AM syntheses (fig. 9). Similar residual porosity after spark plasma sintering is reported in samples prepared by other processes such as ball-milling [43], melt-spinning [10] or solid-state diffusion [44] and seems thus intrinsic to this material densified by SPS.

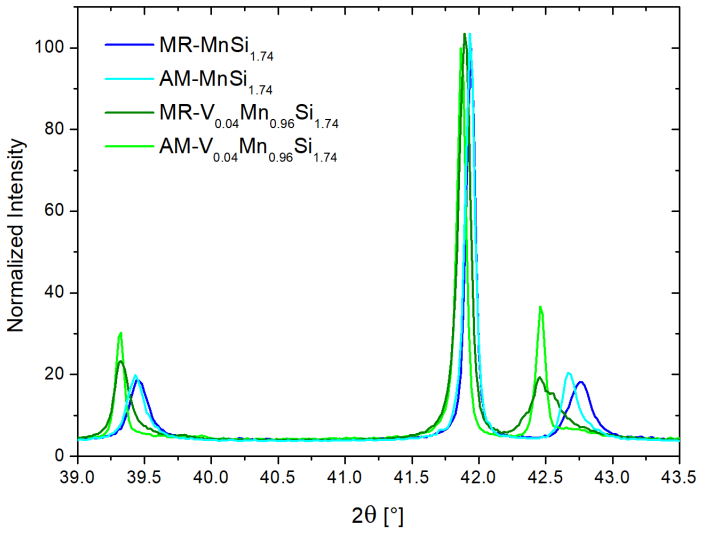

Figure 8: XRD patterns of MR $MnSi_{1.74}$ (dark blue), MR $V_{0.04}Mn_{0.96}Si_{1.74}$ (dark green), AM-$MnSi_{1.74}$ (bright blue) and AM-$V_{0.04}Mn_{0.96}Si_{1.74}$ (bright green) showing the relative peaks shifts among the samples

Further microstructural characterization of the sintered pellets was realized by electron back-scattering diffraction (EBSD, fig.9). EBSD maps have been obtained by scanning the area with a 50 nm step and by indexing the Kikuchi lines using the commensurate Mn_4Si_7 structure ($P\bar{4}c2$, $a = 5.52$ Å , $c = 17.46$ Å). Orientation analysis of the maps do not reveal any crystallographic texturation of the pellets which could have been caused by the uniaxial pressing during the sintering process [23]. TE properties of the pellets will thus be considered as isotropic. The grain size distributions (fig. 9) have been obtained from EBSD maps by considering all diffracting domains containing at least 12 pixels (*i.e.* $\sim$0.03 μm^2). It follows a log-normal law with average values of 580 nm and 606 nm for the sintered undoped and V-doped MR samples, respectively. Such

Table 3: Main structural and microstructural characteristics of the SPSed MR and AM $V_xMn_{1-x}Si_{1.74}$ (x = 0 and 0.04) samples used for the TE characterizations

		MR $MnSi_{1.74}$	AM $MnSi_{1.74}$	MR $V_{0.04}Mn_{0.96}Si_{1.74}$	AM $V_{0.04}Mn_{0.96}Si_{1.74}$
	a (Å)	5.5295(3)	5.52954(6)	5.5308(4)	5.5319(1)
	c_{Mn} (Å)	4.3696(3)	4.36834(8)	4.3710(3)	4.3746(1)
	c_{Si} (Å)	2.5156(3)	2.5110	2.5265	2.5291
	γ	1.7370(3)	1.7397(3)	1.7300(6)	1.7297(1)
Si	A^1(x)	0.0768(8)	0.0769(8)	0.0758(8)	0.0753(6)
	A^2(x)	0.010(1)	0.013(1)	0.012(1)	0.014(1)
	A^3(z)	-0.049(8)	-0.064(7)	-0.042(7)	-0.050(6)
	$U_{iso}(^2)$	0.004(3)	0.008(2)	0.001(2)	0.007(2)
Mn	A^2(z)	-0.017(4)	-0.009(5)	-0.013(4)	-0.009(3)
	$U_{iso}(^2)$	0.001(2)	0.001(1)	0.001(1)	0.001(1)
Impurity	Si	/	2	/	1
(wt. %)	MnSi	/	1	/	1

small grain sizes logically lead to a much higher density of grain boundaries than a conventionally synthesized AM sample with average grain size estimated at 13 μm using the same procedure. Enhanced scattering of the phonons at the grain boundaries and reduced lattice thermal conductivity are expected from such microstructure.

Fig. 10a shows a typical low magnification brighfield TEM image of the MR $MnSi_{1.74}$ densified sample. The shape and size distribution of the grains are in good agreement with the EBSD analysis. The residual porosity due to incomplete densification is confirmed at the grain boundaries. As for the as-synthesized powder, no MnSi precipitates are observed inside the grains after sintering.

As shown on the HRTEM images (fig 10b,c), the great majority of the grain boundaries looks well crystalline and free of amorphous layer. Proper sintering of nanometric powders can be quite challenging because of oxidation layers or residual absorbed species at the surface of the particles which often result in much higher electrical resistivity compared to bulk [45]. In the present case, the good crystallinity of the grain boundaries is expected to prevent exceed-

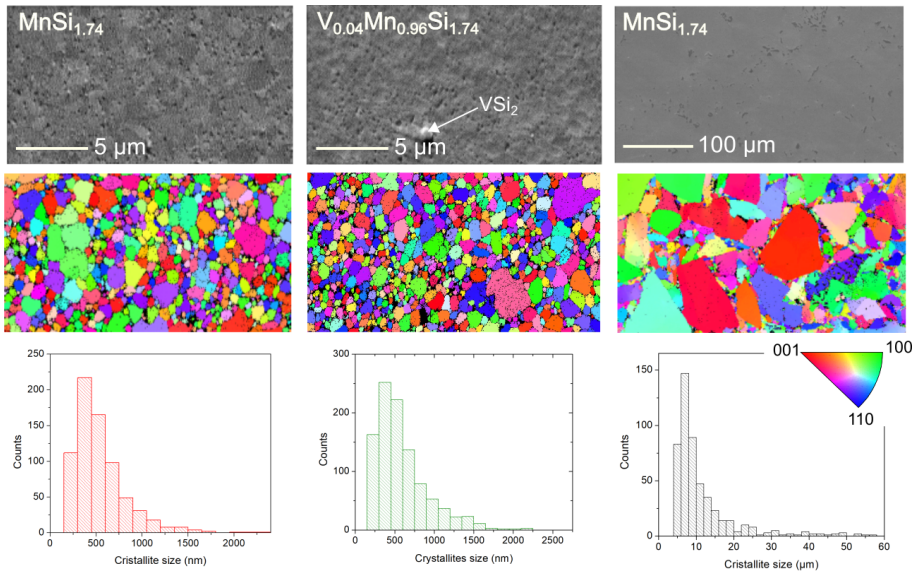

Figure 9: EBSD microstructural analyses of SPSed pellets of MR $MnSi_{1.74}$ (left), MR $V_{0.04}Mn_{0.96}Si_{1.74}$ (middle), and AM $MnSi_{1.74}$ (right). The top, middle and bottom rows correspond to backscattered electron images of the analyzed areas, EBSD maps and histograms of the grain size distribution, respectively

ingly large decrease of the charge carriers transport while still acting as efficient phonon scattering centers.

Typical electron diffraction patterns along the $[\bar{1}20]$ zone axis obtained on a MR $MnSi_{1.74}$ sintered pellet (fig. 10d) are significantly different than those obtained on the as-synthesized powder (fig. 4c). The 'orientation' anomalies affecting the Si and satellite rows of reflections are no more visible. This evolution is attributed to the heat treatment during the sintering and seems correlated to the variation of the modulation vector observed by XRD. Such influence of the temperature on the microstructural properties of $MnSi_{\gamma}$ have already been reported, *e.g.* by Kikuchi *et al.* who reported a linear decrease of γ with temperature above 770 K associated to a VEC change [46]. In addition, careful examination of the diffraction pattern obtained on several areas of the sample reveals some degree of structural heterogeneity between different crystals. As an example, fig. 10e and 10f are diffraction patterns taken along the $[\bar{1}10]$ zone axis on two different crystals. While in fig. 10e the arrangement of the satellite

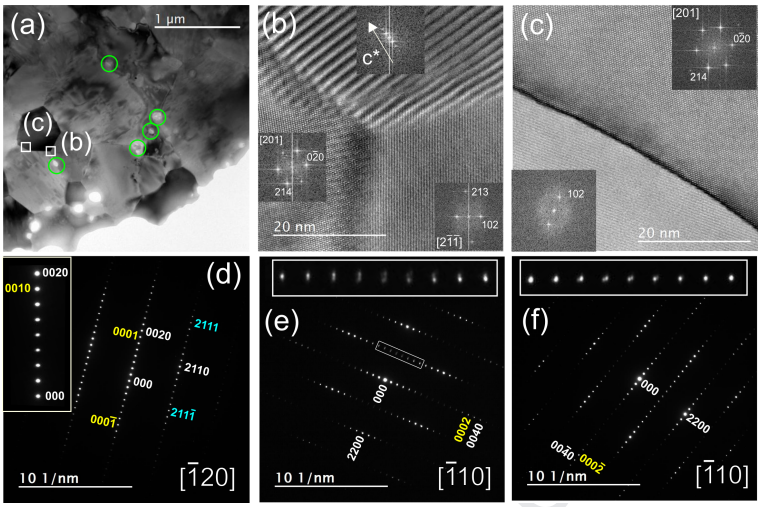

Figure 10: Low magnification brightfield TEM images of typical thinned undoped $MnSi_{1.74}$ pellet showing (a) the residual porosity (encircled in green) and the areas chosen for (b) and (c) HRTEM images showing the high crystallinity of the grain boundaries. FFT in insets indicate the crystal orientation of the grains. (d) Typical electron diffraction pattern taken along the [$\bar{1}$20] zone axis. (e) and (f) Electron diffraction patterns obtained on two different crystals along the [$\bar{1}$10] zone axis showing different anomalies.

peaks is equally spaced but slightly misoriented along the *c*-axis, fig. 10f shows on the contrary a split in satellite spot position in agreement with a variation of the modulation vector. A clear explanation of the origin of such microstructural effects is not available in literature and moreover out of the scope of the present work. However it is worth to underline that such effects are not homogeneous at the micrometer scale throughout the samples and are a characteristic of HMS that should be taken into account during theoretical modeling of the system.

An important contrast inside the crystals can be observed in brightfield mode (fig. 10a) and are attributed to local deviations from the diffraction condition due to large lattice distortions. Magnified images of this area are shown in fig. 11a and 11b revealing high concentration of dislocation-like defects propagating lattice distortion up to a distance of 50 nm in the crystal. A more detailed study of lattice defects was realized by high resolution imaging on thin crystals oriented along the [$\bar{1}$20] zone axis. A defect-free area is shown in fig. 11(c) revealing two types of structural features: (i) large fringes with approximately

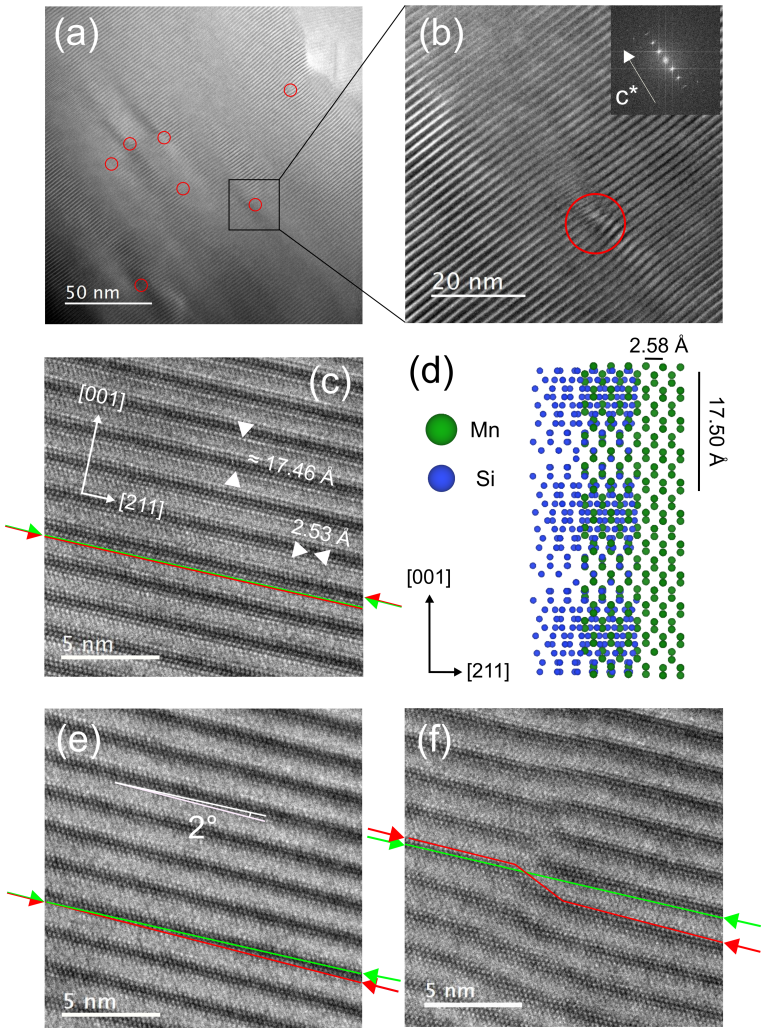

Figure 11: (a) and (b) Brightfield images of MR $MnSi_{1.74}$ sintered pellet showing dislocation-like defects (encircled in red) at two different magnifications. (c) Typical HRTEM image of a defect-free area of a $MnSi_{1.74}$ crystal taken along the [$\bar{1}$20] zone axis with average characteristic distances of the lattice determined from the corresponding FFT image. The orientations of the Moiré fringes and the Mn atomic rows are emphasized on the images with red and green lines, respectively. (d) Scheme of the formation of Moiré-like fringes along the [$\bar{1}$20] direction by interaction of the Si-sublattice (left side) and Mn-sublattice (right side). (e) and (f) HRTEM images showing the tilting of the Moiré fringes relatively to the [211] direction and a dislocation-like defect, respectively.

17.46 Å periodicity along the [001] direction corresponding to the *c*-axis of the commensurate structure of Mn_4Si_7 and generated by Moiré interferences between the two Mn- and Si-subsystems of the composite crystal and (ii) atomic

rows spaced by approximately 2.53 Å along the [211] direction and corresponding to the Mn-Mn distance in the [$\bar{1}$20] projection of the structure (fig. 11c). The schematic representation of the crystal structure projection along the [$\bar{1}$20] direction illustrates the formation of the Moiré fringes by interaction of the two sublattices (fig. 11c). As assumed by the structural model, the orientation of the Moiré fringes and the Mn rows are both parallel to the [211] direction because of the existence of lattice translation symmetry in the (001) plane. Surprisingly, the situation is somewhat different in fig. 11e taken in a different area of the same crystal, where the Moiré fringes are found to be tilted by about 2° with respect to the Mn row itself. Ye and Amelinckx reported similar observations and explained it as a small systematic 'phase-shift' of the Si helical arrangement inside the columnar Mn-sublattice resulting in the tilting of the Moiré fringes [34]. According to these authors, the loss of the tetragonal symmetry in the area of the crystal affected by the Si helices 'phase-shift' explains the 'orientation' anomalies visible on the electron diffraction patterns. Similar type of images taken on the dislocation-like defects (fig. 11f) reveals that only the Moiré fringes are deformed on these areas of the crystal. As shown by the green line, the Mn rows remains well oriented and defect-free throughout the analyzed area and even close to the lattice defect where severe distortion is expected. From these observations, the Si sublattice can be described as highly deformed by numerous defects while on the contrary the Mn lattice remains well crystallized and less affected by Si sublattice disorder. It should be noticed that this more 'realistic' description of the HMS structure is consistent with the peak shape broadening of the Si *hk0m* reflections clearly visible on the powder XRD patterns and supports the use of the strain tensor applied in our Rietveld refinements.

The presence of numerous defects and heterogeneities within the submicronic grains of MR $MnSi_{1.74}$ might act as efficient scattering centers for phonons and thus might strongly influence the thermal conductivity of the materials. In the next section, the thermoelectric properties of pristine and V-doped MR $MnSi_{1.74}$ are thus presented and compared to conventionally synthesized AM

counterparts. The objective is to discuss the effect of the different synthesis routes and microstructures on the TE properties of comparable polycrystalline $MnSi_{1.74}$ samples.

3.5. Thermoelectric properties of MR and AM $MnSi_{1.74}$ and $V_{0.04}Mn_{0.96}Si_{1.74}$

The TE properties of $MnSi_{1.74}$ and $V_{0.04}Mn_{0.96}Si_{1.74}$ synthesized by magnesiore-duction or arc-melting were measured from room temperature up to 800 K (fig. 12). Measurements of the electronic properties were cycled twice and showed good reversibility within a time span of few hours at high temperature.

The electrical resistivity of MR $MnSi_{1.74}$ (fig. 12a) increases from 23 $\mu\Omega$.m at 320 K to 39 $\mu\Omega$.m at 750 K, in agreement with the behavior expected for a heavily degenerated semiconductor. In the same temperature range, its positive Seebeck coefficient (fig. 12b) increases accordingly from 135 to 230 $\mu V.K^{-1}$. The electronic properties of AM $MnSi_{1.74}$ were measured in the same conditions: at room temperature, the electrical resistivity and Seebeck coefficient are found to be 17 % and 2 % lower for the AM $MnSi_{1.74}$ sample in comparison to MR sample. At higher temperature, the difference in electrical resistivity becomes less and less significant, which is attributed to the apparition of the bipolar effect arising at slightly lower temperature (700-750 K) in the case of the MR sample. This effect corresponds to the thermal activation of minor carriers across the band gap (electrons in this case) leading to the simultaneous decrease of the electrical resistivity and the Seebeck coefficient. Maximum power factor *PF* of 1.3 mW m^{-1} K^{-2} at 740 K and 1.4 mW m^{-1} K^{-2} at 700 K (fig. 12c) are found for MR and AM $MnSi_{1.74}$, respectively. This corresponds to a 5 % reduction of the maximum *PF* which can be attributed in a large extent to the higher resistivity of the MR sample. Assuming similar charge carrier concentration in MR and AM samples from equivalent Seebeck coefficients and γ-value [46], the higher electrical resistivity in the mesostructured samples could be explained both by its lower density and possibly by higher scattering of charge carriers at the numerous grain boundaries.

Fig. 12d shows the temperature dependence of the total $\kappa_{tot}(T)$ and lattice $\kappa_L(T)$ thermal conductivities calculated by substracting to $\kappa_{tot}(T)$ the electronic contribution $\kappa_e(T)$ calculated using the Wiedemann-Franz law $\kappa_e(T) = \mathrm{L\,T}/\rho(T)$ with $\mathrm{L} = 2.4.10^{-8}$ W Ω K^{-2}. The lattice thermal conductivity of MR $MnSi_{1.74}$ amounts to 2.3 W m^{-1} K^{-1} at 320 K, which corresponds to a 13 % decrease compared to AM $MnSi_{1.74}$ at the same temperature. The beneficial reduction of the lattice thermal conductivity in MR $MnSi_{1.74}$ is attributed to the smaller grain sizes and the high concentration of defects as evidenced by EBSD and TEM analyses. However, the effect of mesostructuration becomes less and less efficient with increasing temperature and the lattice thermal conductivities of the two samples ultimately reach similar value at 750 K corresponding to the temperature with the highest *PF*. Equivalent maximum *ZT* of about 0.4 is achieved at 750 K which is in good agreement with the best performances reported for undoped HMS synthesized by conventional melting/annealing/SPS [47, 48]. No improvement of the *ZT* could be achieved because the beneficial effect of the mesostructuration on κ_{tot} is counterbalanced by the deterioration of *PF* resulting in equivalent *ZT* values over the whole temperature range. Concordant experimental results show that highly-densified nanostructured HMS (average grain size around 200 nm) synthesized by ball milling followed by SPS did not improve the *ZT* also because of the drop of the power factor [9]. It suggests that any attempt to reduce the grain size down to few hundreds of nm is inefficient to improve *ZT* in the case of $MnSi_{1.74}$.

Increasing *PF* of MR-HMS was attempted by partially substituting manganese with vanadium up to 4 %. Vanadium-doping was reported to effectively improved the power factor of $MnSi_\gamma$ while employing a relatively abundant element compared to other commonly used dopant such as Ge or Re [49]. In addition, V_2O_5 can be reduced relatively easily by Mg in the synthesis condition unlike other very stable oxides such as Al_2O_3. As for undoped $MnSi_{1.74}$, TE measurements were realized on both MR and AM $V_{0.04}Mn_{0.96}Si_{1.74}$. The electrical resistivity and the Seebeck coefficient of both samples decrease with the insertion of vanadium in the structure. This is consistent with an increase of

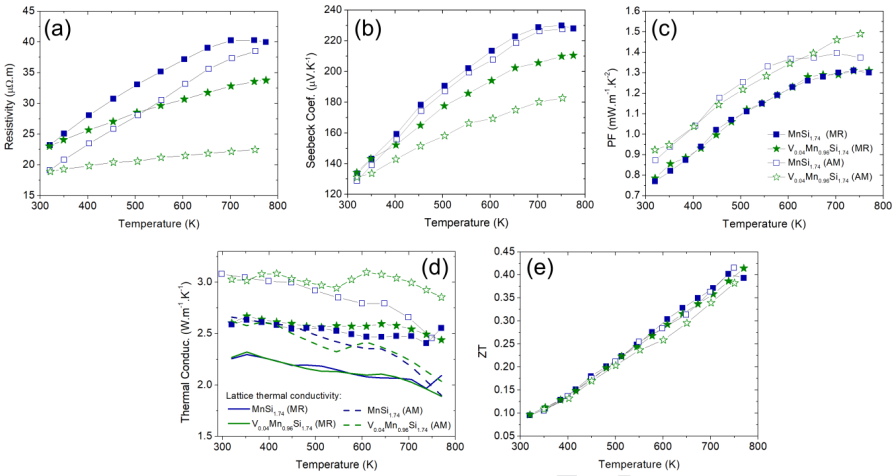

Figure 12: High temperature thermoelectric properties of $MnSi_{1.74}$ (blue squares) and $V_{0.04}Mn_{0.96}Si_{1.74}$ (green stars) synthesized by magnesioreduction (MR, filled symbols) and conventional arc-melting (AM, empty symbols): thermal dependence of (a) electrical resistivity, (b) thermopower, (c) power factor, (d) total (symbols) and lattice (solid lines for MR $MnSi_{1.74}$ and dotted lines for AM $MnSi_{1.74}$) thermal conductivities and (e) resulting figure-of-merit.

the holes concentration in the materials resulting from the substitution of Mn by an electron-poorer element. The less pronounced effect of the doping on the MR sample could be explained by the probable smaller amount of V effectively substituting Mn due to the residual VSi_2 precipitates observed by EDS mapping. Miyazaki *et al.* [49] clearly showed a linear increase of the charge carrier concentration with V-doping. Accordingly, a slightly smaller charge carrier density is expected in the MR-sample, also in agreement with the higher Seebeck coefficient of this material. Consequently, doping the MR sample do not improve *PF* while for the AM sample it leads only to a small improvement of about 8 % above 700 K. Similarly, doping do not induce significant improvement of the lattice thermal conductivity which remain identical to the undoped sample over the whole temperature range. Neither the mass fluctuation scattering of thermal phonons at the disordered Mn/V sites, nor the submicrometric VSi_2 precipitates present in the materials seem to significantly influence κ_L. As a consequence, no improvement of ZT_{max} has been achieved in our case by vanadium doping.

4. Conclusion

A new magnesioreduction synthesis for high purity $MnSi_{1.74}$ is reported. This method offers many advantages over conventional melting/annealing syntheses such as the use of cheap and air-stable precursors (MnO and Si), relatively fast heat treatment at moderate temperature and the possibility to produce doped compounds. Additionally, a finely divided powder is directly obtained, which is suitable for the sintering of mesostructured materials with average grain size of about 500 nm. The influence of the microstructure, investigated by means of EBSD and TEM, on the thermoelectric properties was evaluated by comparison with a sample synthesized by a conventional arc-melting/annealing/sintering process and composed of much larger grains. The thermal conductivity is decreased by up to 25% at 300 K thank to the mesotructuration and associated crystal defect density. However, this beneficial effect is counterbalanced by a decrease of the power factor, resulting eventually in materials with similar $ZT_{max} \simeq 0.4$ at 750 K. The present results suggest that microstructure engineering alone might not be a sufficient strategy to improve the TE properties of HMS.

Acknowledgements

Francis Gouttefangeas is acknowledged for SEM images and EDS analyses performed on the CMEBA platform. TEM experiments were performed on THEMIS platform. Both platforms belong to the ScanMAT unit (UMS 2001, University of Rennes 1) which received a financial support from the European Union (CPER-FEDER 2007-2014). The authors acknowledge support from CREST JPMJCR15Q6 and JSPS KAKENHI JP17H02749, JP16H06441.

References

[1] L. E. Bell, Cooling, heating, generating power, and recovering waste heat with thermoelectric systems, Science 321 (2008) 1457–1461.

[2] I. Petsagkourakis, K. Tybrandt, X. Crispin, I. Ohkubo, N. Satoh, T. Mori,

Thermoelectric materials and applications for energy harvesting power generation, Sci. Technol. Adv. Mater. 19 (2018) 836–862.

[3] L. Aixala, C. de Vaulx, Waste heat recovery by thermoelectricity on passenger car and heavy-duty truck diesel engine: the RENOTER project, 3rd Thermoelectrics Applications Workshop Baltimore, USA (2012) –.

[4] G. Skomedal, L. Holmgren, H. M. andI.S. Eremin, G. Isachenko, M. Jaegle, K. Tarantik, N. Vlachos, M. Manoli, T. Kyratsi, D. Berthebaud, N. Y. D. Truong, F. Gascoin, Design, assembly and characterization of silicide-based thermoelectric modules, Energy Convers. Manag. 110 (2016) 13–21.

[5] T. Mori, Novel principles and nanostructuring methods for enhanced thermoelectrics, Small 13 (2017) 1702013.

[6] J. Mao, Z. Liu, J. Zhou, H. Zhu, Q. Zhang, G. Chen, Z. Ren, Advances in thermoelectrics, Adv. Phys. 67 (2018) 69–147.

[7] D. N. Truong, D. Berthebaud, F. Gascoin, H. Kleinke, Molybdenum, tungsten, and aluminium substitution for enhancement of the thermoelectric performance of higher manganese silicides, J. Electron. Mater. 44 (2015) 3603–3611.

[8] V. Ponnambalam, D. T. Morelli, Effect of addition of the elements Cr, V, Mo, Ge, Re and Ru on the thermoelectric properties of higher manganese silicides $MnSi_{\sim 1.74}$, Mater. Res. Express 6 (2018) 025507.

[9] X. Chen, L. Shi, J. Zhou, J. B. Goodenough, Effects of ball milling on microstructures and thermoelectric properties of higher manganese silicides, J. Alloys Compd. 641 (2015) 30–36.

[10] S. Muthiah, R. C. Singh, B. D. Pathak, P. K. Avasthi, R. Kumar, A. Kumar, A. K. Srivastava, A. Dhar, Significant enhancement in thermoelectric performance of nanostructured higher manganese silicides synthesized employing a melt spinning technique, Nanoscale 10 (2018) 1970–1977.

[11] W. Luo, H. Li, F. Fu, W. Hao, X. Tang, Improved Thermoelectric Properties of Al-Doped Higher Manganese Silicide Prepared by a Rapid Solidification Method, J. Electron. Mater. 40 (2011) 1233–1237.

[12] X. She, X. Su, H. Du, T. Liang, G. Zheng, Y. Yan, R. Akram, C. Uher, X. Tang, High thermoelectric performance of higher manganese silicides prepared by ultra-fast thermal explosion, J. Mater. Chem. C 3 (2015) 12116–12122.

[13] Y. Thimont, L. Presmanes, V. Baylac, P. Tailhades, D. Berthebaud, F. Gascoin, Thermoelectric higher manganese silicides: synthetized, sintered and shaped simultaneously by selective laser sintering/melting additive manufacturing technique, Mater. Lett. 214 (2018) 236–239.

[14] S. Vivès, C. Navone, E. Gaudin, S. Gorsse, Improved microstructure and thermoelectric properties of higher manganese silicide processed by reactive spark plasma sintering, J. Mater. Sci. 52 (2017) 12826–12833.

[15] A. Yamamoto, S. Ghodke, H. Miyazaki, M. Inukai, Y. Nishino, M. Matsunami, T. Takeuchi, Thermoelectric properties of supersaturated Re solid solution of higher manganese silicides, Jpn. J. Appl. Phys. 55 (2016) 020301.

[16] T. Homma, T. Kamata, N. Saito, S. Ghodke, T. Takeuchi, Effects of Re substitution for Mn on microstructures and properties in Re-substituted higher manganese silicide thermoelectric material, J. Alloys Compd. 776 (2019) 8–15.

[17] A. Berche, E. Ruiz-Théron, J.-C. Tedenac, R. Ayral, F. Rouessac, P. Jund, Thermodynamic description of the Mn-Si system: an experimental and theoretical work, J. Alloys Compd. 615 (2014) 693–702.

[18] W. M. Haynes, D. R. Lide, T. J. Bruno, CRC Handbook of Chemistry and Physics, CRC Press Ed. (2015-2016) 6–91.

[19] S. N. Girard, X. Chen, F. Meng, A. Pokhrel, J. Zhou, L. Shi, S. Jin, Thermoelectric properties of undoped high purity higher manganese silicides grown by chemical vapor transport, Chem. Mater. 26 (2014) 5097–5104.

[20] Y. Miyazaki, H. Hamada, K. Hayashi, K. Yubuta, Crystal stucture and Thermoelectric Properties of Lightly Vanadium-Substitued Higher Manganese Silicides $Mn_{(1-x)}V_xSi_\gamma$, J. Electron. Mater. 46 (2017) 2705–2709.

[21] S. S. Ravazi-Tousi, Y.-C. Tseng, Failure analysis and mechanical reliability of cast higher manganese silicide, J. Alloys Compd. 764 (2018) 745–754.

[22] Y. Miyazaki, D. Igarashi, K. Hayashi, T. Kajitani, K. Yubuta, Modulated crystal structure of chimney-ladder higher manganese silicides $MnSi_\gamma$ ($\gamma \approx 1.74$), Phys. Rev. B 78 (2008) 214104.

[23] Y. Sadia, Z. Aminov, D. Mogilyansky, Y. Gelbstein, Texture anisotropy of higher manganese silicide following arc-melting and hot-pressing, Intermetallics 68 (2016) 71–77.

[24] S. Le Tonquesse, E. Alleno, V. Demange, V. Dorcet, L. Joanny, C. Prestipino, O. Rouleau, M. Pasturel, Innovative One-step Synthesis of Mesostructured $CoSb_3$-based Skutterudites by Magnesioreduction, J. Alloys Compd. 796 (2019) 176.

[25] S. N. Girard, T. J. Slade, X. Chen, F. Meng, L. Shi, S. Jin, Nanostructured higher manganese silicides synthesized by magnesioreduction in molten salt fluxes, Abstract book of the 33^{th} Internationnal Conference on Thermoelectrics Nashville, USA.

[26] V. Petříček, M. Dušek, L. Palatinus, Crystallographic Computing System JANA2006: General features, Z. Kristall. 229 (2014) 345–352.

[27] H. J. T. Ellingham, Reducibility of oxides and sulfides in metallurgical processes, J. Soc. Chem. Ind. 65 (1944) 125–160.

[28] O. Knacke, O. Kubaschewski, K. Hesselmann, Thermo-chemical Properties of Inorganic Substances, Springer Ed. vol. II (1991) –.

[29] Z. Zamanipour, X. Shi, M. Mozafari, J. S. Krasinski, L. Tayebi, D. Vashaee, Synthesis, characterization, and thermoelectric properties of nanostructure bulk p-type $MnSi_{1.73}$, $MnSi_{1.75}$, and $MnSi_{1.77}$, Ceram. Int. 39 (2013) 2353–2358.

[30] M. Saleemi, A. Famengo, S. Fiameni, S. Boldrini, S. Battiston, M. Johnsson, M. Muhammed, M. Toprak, Thermoelectric performance of higher manganese silicide nanocomposites, J. Alloys Compd. 619 (2015) 31–37.

[31] Y. Sadia, L. Dinnerman, Y. Gelbstein, Mechanical alloying and spark plasma sintering of higher manganese silicides for thermoelectric applications, J. Electron. Mater. 42 (2013) 1926–1931.

[32] C. Won, H. Nersisyan, H. Won, Titanium powder prepared by a rapid exothermic reaction, Chem. Eng. J. 157 (2010) 270–275.

[33] H. Nersisyan, H. Won, C. Won, A. Joc, J. Kim, Direct magnesioreduction of titanium dioxide to titanium powder through combustion synthesis, Chem. Eng. J. 235 (2014) 67–74.

[34] H. G. Ye, S. Amelinckx, High-resolution electron microscopic study of manganese silicides $MnSi_{2-x}$, J. Solid State Chem. 61 (1986) 8–39.

[35] O. Schwomma, H. Nowotny, A. Wittmann, Die Kristallarten $RuSi_{1.5}$, $RuGe_{1.5}$ und $MnSi_{1.7}$, Monatsh. Chem. 94 (1963) 681–685.

[36] G. Flieher, H. V*ö*llenkle, H. Nowotny, Crystal strucutre of $Mn_{15}Si_{26}$ (manganese silicides of Mn_nSi_{2n-m} type, Monatsh. Chem. 98 (1967) 2173–2179.

[37] H. Knott, M. Mueller, L. Heaton, Crystal structure of $Mn_{15}Si_{26}$, Acta Crystallogr. 23 (1967) 549–555.

[38] S. van Smaalen, Symmetry of composite crystals, Phys. Rev. B 43 (1991) 11330–11341.

[39] V. Petricek, K. Maly, P. Coppens, X. Bu, I. Cisarova, A. Frost-Jensen, The description and analysis of composite crystals, Acta Crystallogr. A 47 (1991) 210–216.

[40] P. M. D. Wolff, T. Janssen, A. Janner, The superspace groups for incommensurate crystal-structures with a one-dimensional modulation, Acta Crystallogr. A 37 (1981) 625–636.

[41] L. Akselrud, R. C. Gil, M. Wagner-Reetz, Y. Grin, Disorder in the composite crystal structure of the manganese 'disilicide' $MnSi_{1.73}$ from powder X-ray diffraction data, Acta Crystallogr. B 71 (2015) 707–712.

[42] E. Teatum, K. Gschneidner, J. Waber, Compilation of calculated data useful in predicting metallurgical behaviour of the elements in binary alloy systems, Los Alamos Scientific Laboratory LA-2345 (1960) –.

[43] Y.-G. Lee, M.-K. Choi, I.-H. Kim, S.-C. Ur, Thermoelectric properties of Nowotny phase, higher manganese silicides synthesized by mechanical alloying process, J. Ceram. Process. Res. 13 (2012) 816–819.

[44] X. Chen, A. Weathers, D. Salta, L. Zhang, J. Zhou, J. B. Goodenough, L. Shi, Effects of (Al,Ge) double doping on the thermoelectric properties of higher manganese silicides, J. Appl. Phys. 114 (2013) 173705.

[45] A. Khan, M. Saleemi, M. Johnsson, L. Han, N. Nong, M. Muhammed, M. Toprak, Fabrication, spark plasma consolidation, and thermoelectric evaluation of nanostructured $CoSb_3$, J. Alloys Compd. 612 (2014) 293–300.

[46] Y. Kikuchi, T. Nakajo, K. Hayashi, Y. Miyazaki, High temperature X-ray diffraction study on incommensurate composite crystal $MnSi_\gamma$ - (3+1)-dimensional superspace approach, J. Alloys Compd. 616 (2014) 263–267.

[47] W. Luo, H. Li, Y. Yan, Z. Lin, X. Tang, Q. Zhang, C. Uher, Rapid synthesis of high thermoelectric performance higher manganese silicide with in-situ formed nano-phase of MnSi, Intermetallics 19 (2011) 404–408.

[48] T.-H. An, S.-M. Choi, W.-S. Seo, C. Park, I.-H. Kim, S.-U. Kim, The effect of microstructure on the thermoelectric properties of polycristalline Higher Manganese Silicides, Jpn. J. Appl. Phys. 52 (2013) 10MC11.

[49] Y. Miyazaki, H. Hamada, H. Nagai, K. Hayashi, Crystal Structure and Thermoelectric Properties of Lightly Substituted Higher Manganese Silicides, Materials 11 (2018) 926.

- Mesostructured higher manganese silicides are synthesized by magnesioreduction
- Crystal structures are refined in composite-incommensurate unit-cells
- Microstructures are examined by EBSD and TEM
- The decrease in thermal conductivity is correlated to the microstructure